Decoupling the Modulus and Toughness Effects of Solid Polymer Electrolytes in All Solid-State Lithium Batteries

*Yongwei Zheng, Xiaowei Li, William R. Fullerton, and Christopher Y. Li**

Department of Materials Science and Engineering, Drexel University, Philadelphia, PA 19104, USA

ABSTRACT. Solid polymer electrolytes (SPEs) have attracted increasing attention for all solid-state lithium battery (ASSLB) applications. Previous SPE design has been focusing on improving polymer shear modulus without sacrificing ionic conductivity, while recent development suggests that other mechanical properties such as elasticity and toughness are also important. Unfortunately, toughness and modulus are often intertwined in SPEs, and the exact role of toughness in SPE performance remains elusive. In this work, we introduce ultra-high molecular weight poly(ethylene oxide) (UHMWPEO) to a PEO-based network SPE to form semi-interpenetrating network (s-IPN) SPEs. This design allows for the s-IPN SPEs to achieve a significant toughness change while retaining similar ionic conductivity and modulus, which effectively decouples the toughness and modulus effects. Our results show that increasing toughness can significantly improve lithium symmetrical battery cycling life. Excellent Coulombic efficiency and full battery

performance have also been achieved. This work therefore demonstrates that toughness should be an important criterion for future SPE design.

KEYWORDS: Solid polymer electrolytes, network solid polymer electrolytes, lithium metal batteries, lithium dendrites, polymer mechanical properties

Introduction

All-solid-state lithium batteries (ASSLBs) employing lithium metal anodes are regarded as the next generation energy storage technology due to the highest theoretical capacity (3860 mAh g^{-1}) and lowest standard potential (-3.04 V vs. SHE) of lithium metal.[1-6] However, growth of lithium dendrites during lithium metal battery (LMB) cycling renders it incompatible with the conventional organic liquid electrolytes (LEs) because the dendritic lithium metal could lead to cell short-circuit, severe thermal runaway and fire hazards.[1-6] Besides, the infinite volume change of lithium metal anode during cycling could break the solid electrolyte interface (SEI), induce side reactions, thicken SEI, and increase the charge transfer resistance.[4-6] Replacing LEs with solid polymer electrolytes (SPEs) that show improved mechanical properties and reduced flammability has been proposed as a critical approach towards safer and higher performance secondary batteries because SPEs typically exhibit good flexibility, processability, ionic conductivity, and lithium dendrite resistance (Table S1).[4, 5, 7-18]

Shear modulus and ionic conductivity are the top two properties to consider when selecting SPEs for lithium battery (LB) applications. Monroe *et al.* demonstrated that when the shear modulus of the electrolytes is over 6.1 GPa, ~1.8 times of Li metal, lithium dendrite growth can be completely

suppressed.[19] This has since become a general guideline for researchers designing new SPE systems. SPEs with various types of polymer chain architectures and microstructures have been reported targeting improved modulus and ionic conductivity.[7-10, 20-23] For example, Stone *et al.* showed that a diblock copolymer SPE, polystyrene-b-poly(ethylene oxide) (SEO), has a shear modulus of 30 MPa and delivers a total charge passed the cell before short-circuit (C_d) close to 190 C cm^{-2} in a symmetrical plating/stripping test at a current density of 0.17 mA cm^{-2}, which is 48 times higher than linear poly(ethylene oxide) (PEO).[24] On the other hand, several works have demonstrated that SPEs with much lower modulus could deliver stable cycling with lithium metal anodes, even at relatively high current densities. Khurana *et al.* synthesized a series of polyethylene (PE)-PEO network SPE with moduli in the range of 0.1-1 MPa. A C_d of 1185 C cm^{-2} at 0.5 mA cm^{-2} was achieved which surpassed the results of the aforementioned block copolymer SPEs.[25] Similar performance was reported in a series of work using hybrid PEO networks.[26-29] Zheng et al. prepared a semi-interpenetrating network (s-IPN) SPE. With a modulus of ~1.77 MPa, this SPE can further improve the cell lifetime of cycling to over 300 h (C_d of 1620 C cm^{-2}) at 1.5 mA cm^{-2}.[30] Most recently, by tuning the network structure, Li et al. fabricated comb-chain crosslinker-based SPEs with a modulus of ~ 2 MPa. Symmetric cells prepared from this SPE delivered near 300 h cycling at 2 mA cm^{-2}.[31] These results suggest that in addition to modulus, other polymer mechanical properties must also play important roles for designing novel SPE systems.

The limitation of using only modulus to describe SPE's mechanical properties lies in that it only describes the deformation behaviour in the elastic region, and often at low deformation. During the operation of a typical LB, the lithium anode front migrates by a few tens of micrometers, totalling a few tens or hundreds of percent of the SPE thickness, which is greater than the elastic region of typical SPEs. Mechanical properties at high deformation regions therefore also need to

be considered. It has been shown that more elastic SPEs owning higher resilience exhibit improved cycling performance.[32] Therefore, SPEs with wider elastic region and greater elongation at break would be desired for LB applications. These two characteristics can be correlated with polymer toughness. While a recent report demonstrated that the cell cycling life scales monotonically with SPE toughness, unfortunately, both modulus and toughness changed significantly in the reported system, and the modulus and toughness effects are therefore intertwined.[31] In this paper, we aim to decouple the modulus and toughness effects on lithium metal battery (LMB) cycling and demonstrate that toughness is another critical mechanical property for SPE design. To this end, we incorporated a series of ultra-high molecular weight linear PEO (UHMWPEO) into a previously reported polyhedral oligomeric silsesquioxane (POSS)-PEO network, as shown in Figure 1.[26-28, 30, 33, 34]

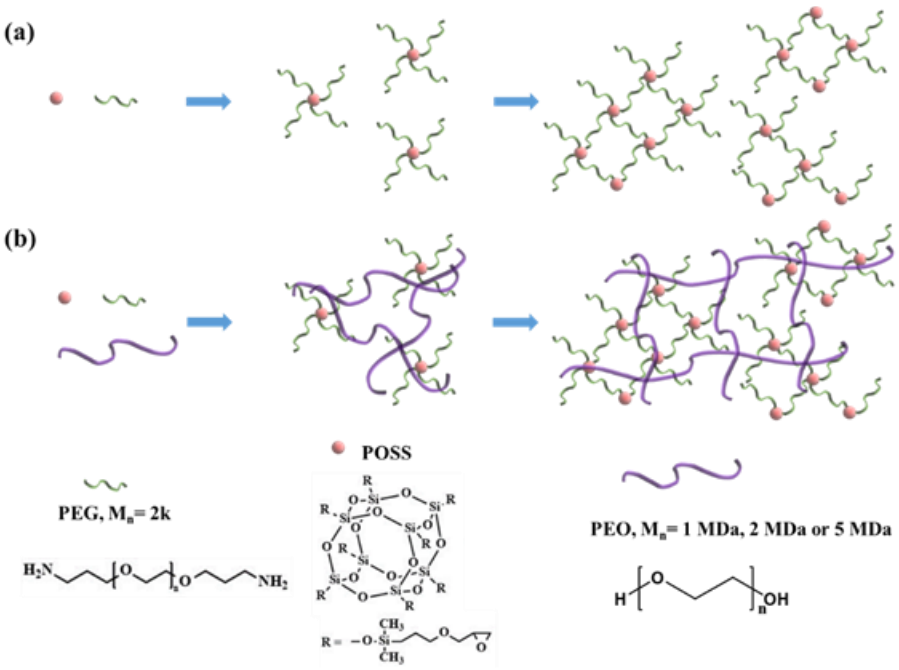

Figure 1. Schematics of the SPE network structure. (a) Networks formed via step-wise growth polymerization. (b) Semi-interpenetrating networks with UHMWPEO. The ultrahigh molecular weight of PEO is designed to improve chain entanglement and network toughness.

The design rationale is two-fold: 1). Polymer rubbery modulus is determined by its entanglement molecular weight (Me), which is 1600 g mol^{-1} for PEO.[35]

$$G = \frac{\rho RT}{M_e} \qquad (1)$$

In eq. (1), G, ρ, R and T are shear modulus, density, gas constant and temperature, respectively. On the other hand, toughness of a polymer is related to the number of entanglement points per chain, and scales with the molecular weight (M_w).[35] Therefore, introducing linear UHMWPEO would increase the toughness without having a significant effect on modulus. Previous work revealed that the effect of M_w on ionic conductivity is mitigated when M_w reaches a threshold.[36, 37] We therefore anticipate moderate effect of UHMWPEO on the SPE's ionic conductivity. The modulus and toughness effects can therefore be decoupled by introducing UHMWPEO into the POSS-PEO network.

Our results showed that significantly improved toughness, from 40 kJ m^{-3} to 500 kJ m^{-3} was achieved in UHMWPEO-containing s-IPNs, while their elastic moduli were maintained in the range of 2.5-3.0 MPa. At the same time, the lithium symmetrical cell cycling time at 1 mA cm^{-2}, 3 mAh cm^{-2} increased from less than 200 h to over 500 h, a 2.5-fold increase. Our design successfully decoupled the effects of modulus and toughness on battery cycling life, and the results demonstrated that toughness played an important role in LMB operation. Moreover, both lithium metal anode cycling Coulombic efficiency test and ASSLBs cycling with lithium iron phosphate (LFP) cathodes revealed improved performance with UHMWPEO, which is attributed to the increased toughness of the SPE.

Experimental Section

Materials: Octa-POSS, poly(ethylene glycol) bis(3-aminopropyl) terminated (M_w = 2000 g mol^{-1}), poly(ethylene oxide) (PEO) (M_w = 1, 2, and 5 MDa), LiTFSI, $LiNO_3$, and dimethylformamide (DMF) were purchased from Sigma-Aldrich. Pristine lithium metal foil was purchased from Alfa Aesar and the thickness is 0.75mm. Carbon black and $LiFePO_4$ was obtained from MTI Corporation. PEO was reprecipitated to remove inhibitors. All other chemicals were used as received.

SPE film preparation: PEG, POSS, PEO and LiTFSI with desired amounts were dissolved in DMF. The molar ratio between PEG and POSS was fixed at 4. The weight percentage of PEO was fixed at 2 *wt.*%. The ratio between EO group and Li^+ was fixed at 16:1. The weight percentage of $LiNO_3$ over total film, if added, was 2 *wt.*%. The solution was stirred at 50 °C for 2 hrs in order to ensure complete mixing before casting the mixed solution on a glass slide. The cast film was transferred into a vacuum oven, cured at 90 °C overnight and then at 120 °C for another 2 hrs. The film was transferred into an Ar-filled glove box once curing was completed. Both oxygen and moisture levels were controlled below 0.5 ppm. The thickness of the prepared films that used for electrochemical tests was controlled at ~70 μm if not specified in the discussion.

Thermal and mechanical characterization: DSC experiments were performed using a TA Instrument Q2000 DSC with Refrigerated Cooling System RCS90 and N_2 purge gas and samples (2-3 mg) were sealed in Tzero pans. The samples were first heated to 90 °C, cooled to -90 °C, and then heated to 90 °C. Heating and cooling rates were both set at 10 °C min^{-1}.

Tensile experiments were performed using the Discovery Hybrid Rheometer-3 (DHR-3). SPE samples were cut into rectangular shape of 15 mm by 5 mm. The thickness of each sample was measured before test. Strain rate was controlled at 10 mm min^{-1}. All samples were tested at 90 °C.

Ionic conductivity: Ionic conductivity was measured by EIS using Princeton Applied Research Parstat 2273 Potentiostat with a Powersuit software. The frequency range was from 1 MHz to 0.1 Hz. SPE films were cut into square shape and sandwiched between two stainless steel electrodes. Temperature varied EIS were measured from room temperature to 100 °C. The bulk resistance of SPE was calculated by fitting an equivalent Randles circuit to the Nyquist plot. Ionic conductivity was determined using equation $\sigma = L/(A \times R)$ where L and A are sample thickness and contact area, respectively. Three batches of each sample were measured, and the average values were reported.

Galvanostatic cycling: Symmetrical cell Li|SPE|Li and asymmetrical cell Li|SPE|Cu were assembled in 2032-type coin cell. The assembled cell was first annealed in oil bath at 90 °C for 4 hrs and then galvanostatic cycled using Arbin battery tester at 90 °C. All cell assembly process was finished in Ar-filled glove box. For the symmetrical cell, the current density of J = 1 mA cm^{-2} was applied, and the areal capacity of both plating and stripping was controlled at 3 mAh cm^{-2}. For the asymmetrical cell, the current density of 0.5 mA cm^{-2} was applied. The areal capacity of lithium plating on Cu working electrode was controlled at 0.5 mAh cm^{-2}. The cut-off voltage of lithium stripping from Cu working electrode was 1 V.

Solid-state battery testing: The composite LFP cathode was fabricated by LFP/binder/carbon black with a weight ratio 60/28/12. The SPE binder used a PEG(6 kDa) to POSS molar ratio of 2:1 and EO to LiTFSI of 16:1. PEG, POSS and LiTFSI were first dissolved in a small amount of THF, and pre-polymerized at 60 °C for 3 hrs. THF and distilled water were then added to the binder precursor solution at 3/2 (vol/vol). LFP and carbon black were then mixed in the binder precursor

solution, stirred at 50 °C for 2 hrs and sonicated before use. The obtained slurry was casted on stainless steel sheet, cured and dried at 120 °C overnight. Active material loading for each cathode was 2-3 mg. The full battery was assembled by sandwiching the SPE with the prepared composite LFP cathode and Li metal anode. The batteries were cycled at 90 °C in a 2.5-3.8 V potential window. Current rate was determined by the theoretical capacity of LFP which is 170 mAh g^{-1}. All batteries were annealed in oil bath at 90 °C for 4 hrs before cycling.

Results and discussion

Physical properties of UHMWPEO-containing network SPEs

The s-IPN SPEs were synthesized by one-pot polymerization. In brief, amine end-terminated poly (ethylene glycol) (PEG, molar mass of 2 kDa) was crosslinked by epoxy end-functionalized POSS in the presence of UHMWPEO and bis(trifluoromethanesulfonyl)imide (LiTFSI). To avoid phase separation, the monomers and LiTFSI were dissolved in dimethylformamide (DMF) and the polymerization was initiated in solution state. The molar ratio between PEG and POSS was fixed at 4:1 and 16:1 between ethylene oxide (EO) and LiTFSI, since the resultant SPEs show excellent overall modulus, ionic conductivity, and LMB performance.[26, 34] UHMWPEO with molar mass of 1, 2, and 5 MDa were added to the network and the concentration was fixed at 2 wt.%. UHMWPEO-free PEG-POSS network was prepared as the control. Samples are abbreviated as SPE-*n*PEO where n denoted as the molar mass of UHMWPEO (the unit is MDa). Table 1 and Table S2 summarize the physical properties of the prepared samples.

Table 1. Physical properties of prepared SPEs.

SPEs	EO [wt. %][a]	T_g [°C][b]	X_c [%][c]	σ [S cm^{-1}] at 30 °C	σ [S cm^{-1}] at 90 °C	*Young's modulus* [MPa] at 90 °C	*Toughness* [KJ m^{-3}] at 90 °C
SPE-0PEO	61.0	-45.5	/	3.4×10^{-5}	6.3×10^{-4}	2.41	41.3
SPE-1PEO	61.3	-44.6	1.94	2.0×10^{-5}	6.1×10^{-4}	2.70	143.7
SPE-2PEO	61.3	-44.4	2.67	1.3×10^{-5}	4.4×10^{-4}	2.98	222.7
SPE-5PEO	61.3	-45.9	1.02	1.2×10^{-5}	4.0×10^{-4}	2.87	496.6

a Weight percent of PEG and PEO over the total SPE (salt included).

b Measured by DSC and calculated from the second heating thermograms.

c Normalized by eq. (2). Melting enthalpy was measured by DSC thermograms of the second heating.

Differential scanning calorimetry (DSC) was used to characterize the thermal properties of SPEs. Figure 2(a) shows the thermograms of SPE-0PEO, SPE-1PEO, SPE-2PEO and SPE-5PEO from the second heating scan to avoid thermal history. For SPE-0PEO, the glass transition temperature (T_g) was detected at -45.5 °C. No melting peak was detected, as covalent crosslinking effectively suppressed crystallization. SPE-1PEO, SPE-2PEO and SPE-5PEO have T_g of -44.6 °C, -44.4 °C and -45.9 °C, respectively. This suggests that incorporating UHMWPEO has little effect on the network T_g. On the other hand,

recrystallization at ~ 0 °C and melting peaks at ~ 25 and 50 °C were observed for all three samples. The degree of crystallinity (X_c) normalized by the PEO content is calculated based on the enthalpy melting and given by equation (2).

$$Xc = \frac{\Delta H_m}{\Delta H_{m_0} \omega} \times 100\% \qquad (2)$$

ΔH_m is enthalpy of the melting peak from DSC. ΔH_{m_0} is the enthalpy of melting from 100% PEO crystalline, which is 196.6 J g^{-1}.[38] ω is the PEO weight content. When calculating ΔH_m, recrystallization exotherm were subtracted from the melting exotherm so that the crystallinity calculated reflects samples before second heating.

DSC thermograms of the pure UHMWPEO, denoted as PEO1, PEO2 and PEO5 are shown in Figure S1. PEO1, PEO2 and PEO5 show the melting temperature (Tm) of 61.5 °C, 66.8 °C, and 61.0 °C, respectively. The Xc are 77.3%, 71.0%, and 79.7%. A weak glass transition was also detected at well below -50 °C. When the pure PEO is blended with LiTFSI (EO:Li=16), the PEO SPE was abbreviated as PEOn-SPE where n denoted as the Mw of PEO. Figure S2 show the DSC curves of the three PEO-SPE. PEO1-SPE, PEO2-SPE and PEO5-SPE show the Xc of 19.9%, 25.8%, and 11.0%. The corresponding Tgs are -42.4 °C, -42.4 °C, and -47.8 °C. Comparing with linear UHMWPEO SPEs, SPE-nPEO show much lower degree of crystallinity, confirming that chemical crosslinking reduces polymer crystallization.

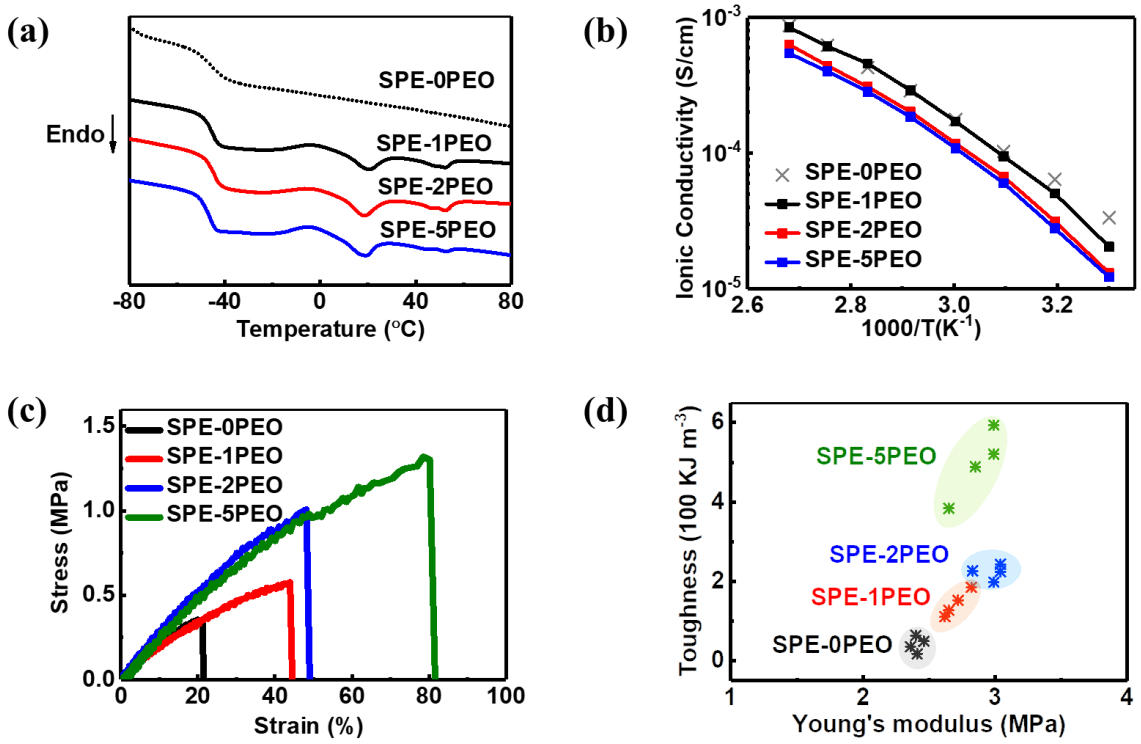

Figure 2. (a) DSC thermograms of prepared SPEs. The scanning rate is 10 °C min-1 and the data is from the second heating profile. (b) Ionic conductivity of the SPEs as a function of temperature. (c) Stress-strain profiles from tensile test for SPE-0PEO, SPE-1PEO, SPE-2PEO, and SPE-5PEO. The strain rate is 10 mm min-1 and the ambient temperature is 90 °C. (d) The distribution of toughness and Young's modulus for the SPEs. Each data point represents one measurement.

Figure 2(b) shows the temperature-dependent ionic conductivity of the SPEs. The conductivity of SPE-0PEO can reach 3.4×10-5 S cm^{-1} at 30 °C. While the conductivity of SPE-1PEO, SPE-2PEO and SPE-5PEO slightly decreases to 2.0×10^{-5}, 1.3×10^{-5}, and 1.2×10^{-5} S cm^{-1} at 30 °C, respectively. This might be due to long chain nature of

UHMWPEO and the crystalline phases in the s-IPN SPEs. At 90 °C, the conductivity of SPE-0PEO, SPE-1PEO, SPE-2PEO and SPE-5PEO is 6.3×10^{-4}, 6.1×10^{-4}, 4.4×10^{-4}, and 4.0×10^{-4} S cm^{-1} at 90 °C. To avoid the effect of crystallization and achieve the high conductivity, the following characterization was conducted at 90 °C. Note that the conductivities of the network SPEs are similar to the UHMWPEO-based linear SPEs (Figure S3). More importantly, the ionic conductivity of the three network SPEs are relatively similar, which is critical for delineating the toughness effect of Young's modulus and toughness of the samples were measured using tensile testing at 90 °C. The stress-strain curves of each sample are shown in Figure 2(c). Four samples were measured for each SPE. Young's modulus was calculated by fitting the slope of stress-strain curve in the elastic region and toughness was estimated by integrating the area under the stress-strain curve. SPE-0PEO shows a Young's modulus of 2.41 MPa. In an ideal condition, the M_e of SPE-0PEO is equal to the length between each crosslinking point which should be the M_w of PEG, 2000 g mol^{-1}. the Young's modulus (E) of SPE-0PEO can be estimated based on

$$E = 2G(1 + \nu) \qquad (3)$$

Where ν is Poisson's ratio. This leads to an E of 5.43 MPa at 90 °C (ρ= 1.2 g cm^{-3}, ν= 0.499), which is higher than the measured value.[39] The discrepancy can be attributed to defects in the SPE-0PEO network and the plasticizing effect of lithium salt. When UHMWPEO was added, the modulus slightly increased to 2.70 MPa, 2.98 MPa and 2.87 MPa, for SPE-1PEO, SPE-2PEO and SPE-5PEO, respectively. The moduli of the three SPEs are relatively similar, all slightly higher that the SPE-0PEO control, likely due to the higher intrinsic rubbery moduli of UHMWPEO.

The long polymer chain of UHMWPEO effectively increases the SPE's elongation at break and toughness, as shown in Figure 2(c). SPE-5PEO has a toughness of 496.6 KJ m^{-3}, which is over tenfold higher than SPE-0PEO (41.3 KJ m^{-3}). SPE-1PEO and SPE-2PEO also show moderately improved toughness of 143.7 KJ m^{-3} and 222.7 KJ m^{-3}, respectively. Figure 2(d) summarize the Young's modulus and toughness of the SPEs. The property distribution clearly illustrates drastic differences in toughness and relatively constant modulus among all the samples; decoupling of modulus and toughness was therefore successfully achieved in our system.

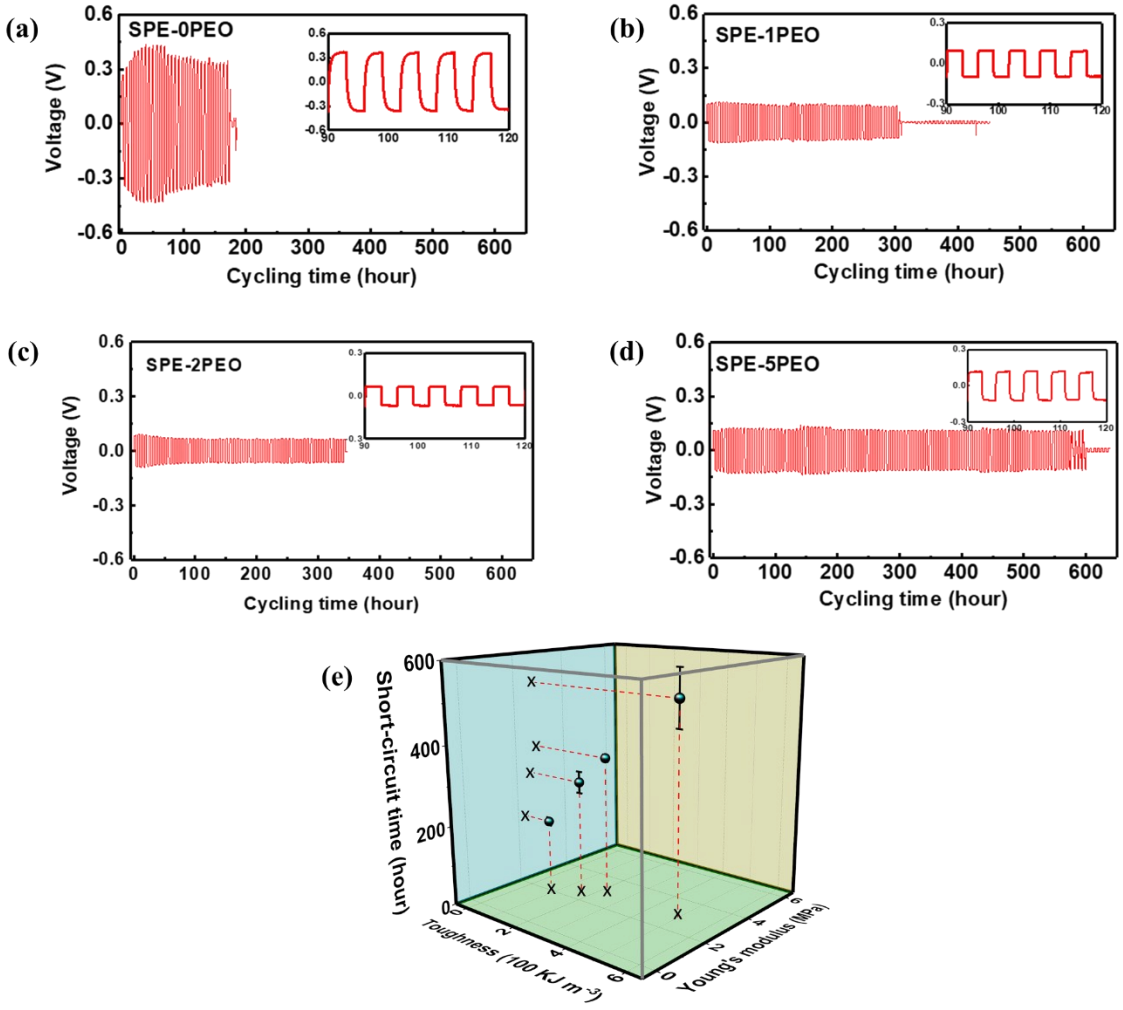
(a)
SPE-0PEO
Voltage (V)
Cycling time (hour)
(b)
SPE-1PEO
Voltage (V)
Cycling time (hour)
(c)
SPE-2PEO
Voltage (V)
Cycling time (hour)
(d)
SPE-5PEO
Voltage (V)
Cycling time (hour)
(e)
Short-circuit time (hour)
Toughness (/100 KJ m-3)
Young's modulus (MPa)
(f)
Li
SPE
Li
50 μm
(g)
2 μm
(h)
Li
SPE
Li
50 μm
(i)
2 μm

Figure 3. Galvanostatic Li|SPE|Li symmetrical cells cycling profiles of (a) SPE-0PEO, (b) SPE-1PEO, (c) SPE-2PEO, and (d) SPE-5PEO. The current density and areal capacity are 1 mA cm^{-2} and 3 mAh cm^{-2}, respectively. The ambient temperature is 90 °C. The insets are zoomed-in profiles between 90 h- 120 h. (e) 3-D plot of the symmetrical cell cycling short-circuit time with the variables of SPEs' Young's moduli and toughness. Cross-sectional SEM images of (f-g) SPE-0PEO and (h-i) SPE-5PEO. The images were taken after cell short-circuit. The white dashed line is the boundary of Li metal and SPE, and the white dashed circle marks the area of dendrites.

Electrochemical properties of UHMWPEO-containing network SPEs

Li^+ transference number of SPE-5PEO was measured using the previously reported potentiostatic polarization method (Figure S4).[12] The Li^+ transference number is 0.24 which is consistent with our previous results.[26] Linear sweep voltammetry (LSV) was conducted on SPE-5PEO using the cell configuration of Li|SPE-5PEO|stainless steel (Figure S5). The oxidation current can be observed at around 4.25V which is within the range of reported ether-based SPEs.[26, 29, 40]

Galvanostatic lithium plating/stripping tests with a Li|SPE|Li symmetrical cell configuration were utilized to evaluate the SPE cycling stability. The thicknesses of all samples were controlled to be ~ 100 μm since the cycling performance is SPE thickness-dependent.[41] A current density of 1 mA cm^{-2} and an areal capacity of 3 mAh cm^{-2} were applied to each cell and the temperature was controlled at 90 °C. Figures 3(a-d) show the voltage profiles of SPE-0PEO, SPE-1PEO, SPE-2PEO, and SPE-5PEO, respectively. Short-circuit is defined as when the voltage suddenly dropped to ~ 0 V. The total cycling time before short-circuit is defined as the short-circuit time (t_{sc}). The t_{sc}

of the cell using SPE-0PEO reaches 170 h which is consistent with our previous report.[26] When UHMWPEO is incorporated, the short-circuit time gradually increases with the Mw of UHMWPEO. SPE-1PEO, SPE-2PEO and SPE-5PEO deliver a stable t_{sc} of 283h, 351h, and 521 h, indicating that compared with SPE-0PEO, the short-circuit time is improved by 66%, 106% and 206%, respectively. These results compare favorably with reported SPE systems as shown in Table S1, particularly at high current densities. Besides, the overpotential is suppressed with UHMWPEO. The inset figures of Figure 3(a-d) show the high-resolution voltage profiles between 90-120 h cycling. The overpotential of the cell using SPE-0PEO reaches over 0.3 V while the overpotentials of the three UHMWPEO-containing cells are all below 0.15 V. The lower overpotential is likely due to the intimate SPE-lithium contact in high M_w samples. The high toughness of the SPE also enables a conformal coating of the electrolyte onto the lithium metal/dendrites surface and thus mitigates interface resistance. Figure 3(e) shows the correlation between the SPE's toughness, Young's modulus, and short-circuit time, which demonstrates that while the modulus is relatively constant, toughness plays a critical role in enhancing the short-circuit time.

To further study the short-circuit mechanism and the role of SPEs, scanning electron microscopy (SEM) was used to observe the cross-sectional morphology of symmetrical cells. Symmetrical cells using SPE-0PEO and SPE-5PEO were dissembled after short-circuiting. Figure 3(f-g) show the SEM images of the cell using SPE-0PEO. The SPE film was broken down into several residual pieces. The enlarged image in Figure 3(g) shows the lithium dendrites have penetrated the SPE, and SPE|Li^0 interface is loosely detached. This suggests that, during cycling, the SPE film was gradually broken, delaminated from the Li^0 anode surface. On the other hand, Figures 3(h-i) show the cross-section images of the cell using SPE-5PEO. Although short-circuited, the SPE film still

shows uniform morphology and tight adhesion to the lithium metal surface. The trace of lithium dendrites penetration pathway can be detected on the enlarged image of Figure 3(i). Pieces of lithium residuals are also observed which can be attributed to the orphaned lithium from the dendrites. Since SPE-5PEO exhibited the best performance in mechanical properties and cycle life, it was selected for further electrochemical characterization.

A high Li^0 anode cycling Coulombic efficiency (CE) is critical to realizing anode-free batteries and downsizing the anode volume, which is a major challenge for LMBs. In this work, we used asymmetrical cells with a Cu|SPE|Li configuration to evaluate the Li^0 anode cycling efficiency. The Cu^0 foil was used as working electrode and Li^0 was used as both the counter and reference electrodes. During the discharging process, lithium was plated onto the Cu foil at 0.5 mA cm^{-2} for 1 h. During the charging process, the plated lithium was stripped back at 0.5 mA cm^{-2} until the voltage reached 1 V. CE was calculated by dividing the charge passed in stripping by that in plating. According to our previous work, CE of the cell using SPE-0PEO suddenly drops after 55 cycles. The average CE of the first 50 cycles is 82.0% ± 15.4%.[29] Figure 4(a) shows the CE of the cell using SPE-5PEO. The cell was tested for 100 cycles with an average CE of 85.8% ± 5.4%. Figure 4(b) shows the voltage profiles of the cell using SPE-5PEO from the 10^{th} cycle and 50^{th} cycle. The voltage hysteresis slightly changes from 237 mV to 268 mV. On the other hand, the voltage hysteresis of the cell using SPE-0PEO significantly increases from 205 mV to 573 mV (Figure S6). The lower voltage hysteresis is attributed to the weak interface polarization benefited from the improved elasticity in SPE-5PEO, which allows for better conformal contact between SPE and the electrode.

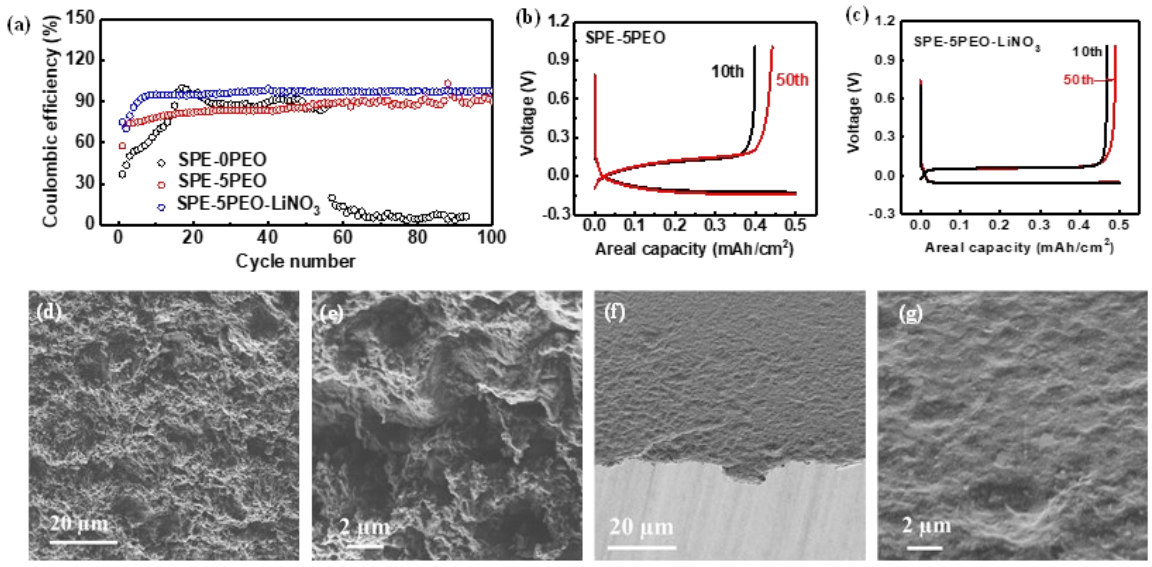

Figure 4. (a) Comparison of CE of lithium plating/stripping on Cu electrode using the electrolytes of SPE-0PEO, SPE-5PEO, and SPE-5PEO-$LiNO_3$. The data points of SPE-0PEO is reproduced from Zheng, Y.; Li, X.; Fullerton, W. R.; Qian, Q.; Shang, M.; Niu, J.; Li, C. Y., Interpenetrating Network-Based Hybrid Solid and Gel Electrolytes for High Voltage Lithium Metal Batteries. *ACS Appl. Energy Mater.* **2021,** *4(6)*, 5639-5648. Copyright 2021 American Chemical Society.[29] The current density and plating areal capacity are 0.5 mA cm^{-2} and 0.5 mAh cm^{-2}. The ambient temperature is 90 °C. Voltage profiles of (b) SPE-5PEO and (c) SPE-5PEO-$LiNO_3$ at the 10^{th} (black) and 50^{th} (red) cycles. Top-view SEM images on Cu electrode after 100 cycles of (d-e) SPE-5PEO and (f-g) SPE-5PEO-$LiNO_3$.

A CE of 85.8%, although quite high in SPEs, is still inferior to ideal anode performance. Introducing UHMWPEO to SPEs can only tune the SPE mechanical properties. Our previously reported interpenetrating network SPE, incorporating poly(acrylonitrile) (PAN) into PEO network,

exhibited a CE of 89.6% ± 2.3%.[29] Other literature reports using LEs demonstrated that CE can reach over 95% for bare or protected lithium metal anodes.[42-44] To further improve the anode cycling efficiency, 2 *wt*.% of lithium nitrate ($LiNO_3$) was infiltrated into SPE-5PEO as the additive as $LiNO_3$ can quickly be reduced and form a dense, mechanically and electrochemically stable SEI on lithium metal anodes.[45, 46] The resultant SPE is abbreviated as SPE-5PEO-$LiNO_3$. Figures 4(a) and (c) show the CE and voltage profiles of the cell using SPE-5PEO-$LiNO_3$ as the electrolyte. With the addition of $LiNO_3$, the CE is improved to 96.0% ± 4.2% for 100 cycles. The voltage hysteresis of the 10th cycle and 50th cycle are 114 mV and 112 mV, which are less than half of its SPE-5PEO counterpart. Besides, the plating overpotential of the 50th cycle decreases from 139 mV to 56 mV upon adding $LiNO_3$. These results are outstanding in SPE systems and can compete with some of the LE systems. For example, Liu et al. reported an average CE of 97.6% for 120 cycles in 1,3-dioxolane/dimethoxy ethane (DOL/DME) LEs at 0.5 mA cm^{-2} with Silly Putty coated electrode.[42] Zhu et al. showed an average CE of 94.5% for 200 cycles in DOL/DME electrolyte at 0.5 mA cm^{-2} with poly (dimethylsiloxane)-coated electrode,[44] whereas a bare electrode using DOL/DME can only be stably cycled for 75 cycles and the CE drops below 90%.[44] $LiNO_3$ was utilized as the additive in all the above systems. Those reports illustrated that the significance of both polymer coating and $LiNO_3$ additive. The polymer coating is aimed to mechanically stabilize the interface while $LiNO_3$ is utilized to create a more chemically stable interface. SPE-5PEO-$LiNO_3$ therefore fulfilled both of the requirements. Figures 4(d-g) show the top-view SEM images of the lithium metal plated onto the Cu foil after 100 cycles. The surface morphology is much smoother for the cell using SPE-5PEO-$LiNO_3$ (f-g).[3] $LiNO_3^-$ free SPE-5PEO shows relatively rougher surface, while no large dendrites or nucleation sites were observed. The roughness is likely originated from the non-ideal SEI failure during the cycling.

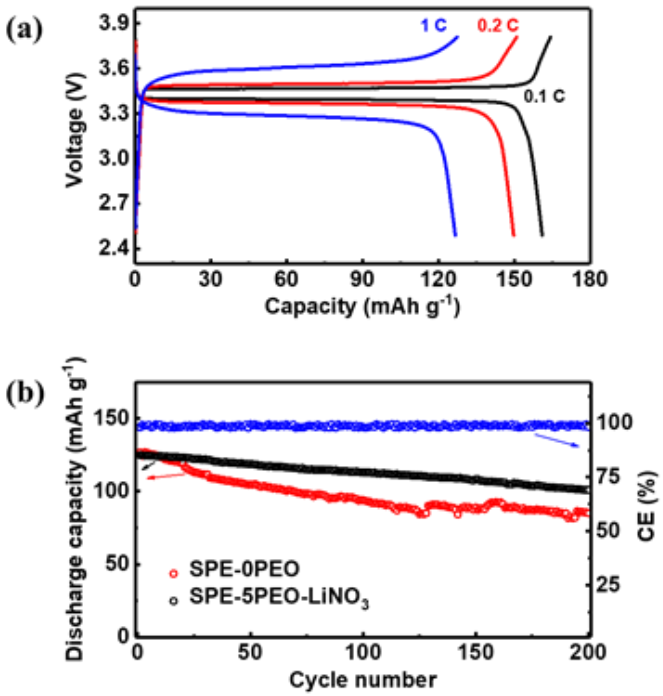

Figure 5. LFP solid state battery performance with SPEs and lithium metal anode. All cells were cycling at 90 °C. (a) Initial charge /discharge profiles at different C rate of cells using SPE-5PEO-$LiNO_3$. (b) Comparison of the cycling stability of cells using SPE-0PEO (black) and SPE-5PEO-$LiNO_3$ (red) at 1 C. The CE (blue) is from the cell using SPE-5PEO-$LiNO_3$.

Lithium iron phosphate (LFP) was selected as the cathode active material and coupled with SPE-5PEO-$LiNO_3$ and lithium metal anode to evaluate battery performance. The battery using SPE-0PEO was also assembled as control. All batteries were galvanostatic cycled between 2.5 V – 3.8 V at 90 °C. Figure 5(a) shows the charge and discharge capacity at different C rates for the battery using SPE-5PEO-$LiNO_3$ as the SPE. The calculation of C rate is based on the theoretical specific capacity of LFP (170 mAh g^{-1}).[47] A discharge capacity of 161 mAh g^{-1}, 150 mAh g^{-1} and 127 mAh g^{-1} can be delivered at 0.1 C, 0.2 C and 1 C, respectively. Those are consistent with our previously reported results.[26-28, 30, 33] For example, the single network POSS-2PEG6k delivers an initial

discharge capacity of 135 mAh g^{-1} at 1 C.[26] The absolute value of the initial capacity, especially at high C rate is determined by the charge-transfer and electrode reaction kinetics which are related to the ionic conductivity and cathode microstructure. SPE-5PEO-$LiNO_3$ SPE performs similar in rate capability compared with these previous reported systems. However, the higher toughness and stable SEI of SPE-5PEO-$LiNO_3$ demonstrate its superior performance in long time cycling. Figure 5(b) shows the evolution of discharge capacity with cycle number at 1 C. After 200 cycles, the cell using SPE-5PEO-$LiNO_3$ can still deliver a capacity of 101 mAh g^{-1} and the capacity retention rate is 74.8% with an average CE of 98.7%. While the capacity of cells using SPE-0PEO decreases from 128 mAh g^{-1} to 85 mAh g^{-1} and only 66.4% of the capacity left after 200 cycles. Table S1 summarizes the battery performance of recently reported SPE systems, and SPE-5PEO-$LiNO_3$ stands out with 200 cycles at 1C. Besides, the profile of capacity-cycles is less stable for the battery using SPE-0PEO. These results demonstrated that incorporation of UHMWPEO and $LiNO_3$ does significantly improve the battery cycling performance.

Conclusions

The elastic modulus and toughness effects of SPEs in LMB cycling were successfully decoupled by incorporating linear UHMWPEO into crosslinked PEO network. Over tenfold increase of toughness was achieved while the elastic modulus and conductivity were maintained relatively unchanged. The observed symmetrical cell performance in lithium dendrite resistance tests was then attributed to the SPE toughness effect. In our experiments, a threefold increase in cycling time in Li|SPE|Li symmetric cells was achieved, demonstrating the significance of toughness in suppressing lithium dendrite growth. Cross-sectional SEM revealed the effect of high toughness on maintaining network structure integrity over cycling. The benefit of high toughness SPEs is

likely associated with the intimate SPE/lithium contact during cell cycling. Furthermore, we showed that SPE-5PEO-$LiNO_3$ delivered a high CE in lithium metal anode cycling which can compete with LE-based systems. Therefore, pursuing high toughness with good elasticity is a new critical direction for future SPE design.

ASSOCIATED CONTENT

Supporting Information. The following files are available free of charge. DSC results; conductivity data; symmetrical cell voltage profile, LSV and transference number testing restuls.

AUTHOR INFORMATION

Corresponding Author

*Corresponding author: Chrisli@drexel.edu, orcid.org/0000-0003-2431-7099

Author Contributions

YZ designed and conducted the experiments, wrote the manuscript. XL and WRF conducted materials characterization and results discussion. CYL directed the research. The manuscript was written through contributions of all authors. All authors have given approval to the final version of the manuscript.

Notes

There are no conflicts to declare.

ACKNOWLEDGMENT

We are grateful for the support from the National Science Foundation through Grants CBET 1603520 and CBET 2033882.

REFERENCES

1. Goodenough, J. B.; Kim, Y., Challenges for rechargeable Li batteries. *Chem. Mater.* **2009,** *22* (3), 587-603.
2. Xu, W.; Wang, J.; Ding, F.; Chen, X.; Nasybulin, E.; Zhang, Y.; Zhang, J.-G., Lithium metal anodes for rechargeable batteries. *Energy Environ. Sci.* **2014,** *7* (2), 513-537.
3. Cheng, X.-B.; Zhang, R.; Zhao, C.-Z.; Zhang, Q., Toward safe lithium metal anode in rechargeable batteries: a review. *Chem. Rev.* **2017,** *117* (15), 10403-10473.
4. Lopez, J.; Mackanic, D. G.; Cui, Y.; Bao, Z., Designing polymers for advanced battery chemistries. *Nat. Rev. Mater.* **2019,** *4* (5), 312-330.
5. Tikekar, M. D.; Choudhury, S.; Tu, Z.; Archer, L. A., Design principles for electrolytes and interfaces for stable lithium-metal batteries. *Nat. Energy* **2016,** *1* (9), 16114.
6. Choudhury, S.; Stalin, S.; Vu, D.; Warren, A.; Deng, Y.; Biswal, P.; Archer, L. A., Solid-state polymer electrolytes for high-performance lithium metal batteries. *Nat. Commun.* **2019,** *10* (1), 4398.
7. Manthiram, A.; Yu, X.; Wang, S., Lithium battery chemistries enabled by solid-state electrolytes. *Nat. Rev. Mater.* **2017,** *2* (4), 16103.
8. Zhao, Q.; Stalin, S.; Zhao, C.-Z.; Archer, L. A., Designing solid-state electrolytes for safe, energy-dense batteries. *Nat. Rev. Mater.* **2020**, 1-24.
9. Armand, M., Polymer solid electrolytes - an overview *Sol. St. Ion.* **1983,** *9-10* (DEC), 745-754.
10. Yang, C.; Fu, K.; Zhang, Y.; Hitz, E.; Hu, L., Protected Lithium-Metal Anodes in Batteries: From Liquid to Solid. *Adv. Mater.* **2017,** *29* (36), 1701169.
11. Fenton, D.; Parker, J.; Wright, P., Complexes of alkali metal ions with poly (ethylene oxide). *Polymer* **1973,** *14* (11), 589.
12. Bruce, P.; Vincent, C., Polymer electrolytes. *J. Chem. Soc., Faraday Trans.* **1993,** *89* (17), 3187-3203.
13. Hallinan Jr, D. T.; Balsara, N. P., Polymer electrolytes. *Ann. Rev. Mater. Res.* **2013,** *43*, 503-525.
14. Meyer, W. H., Polymer electrolytes for lithium-ion batteries. *Adv. Mater.* **1998,** *10* (6), 439-448.
15. Brissot, C.; Rosso, M.; Chazalviel, J. N.; Lascaud, S., Dendritic growth mechanisms in lithium/polymer cells. *J. Power Sources* **1999,** *81*, 925-929.
16. Rosso, M.; Brissot, C.; Teyssot, A.; Dolle, M.; Sannier, L.; Tarascon, J. M.; Bouchetc, R.; Lascaud, S., Dendrite short-circuit and fuse effect on Li/polymer/Li cells. *Electrochim. Acta* **2006,** *51* (25), 5334-5340.

17. Dolle, M.; Sannier, L.; Beaudoin, B.; Trentin, M.; Tarascon, J. M., Live scanning electron microscope observations of dendritic growth in lithium/polymer cells. *ECS Sold State Lett.* **2002,** *5* (12), A286-A289.
18. Harry, K. J.; Hallinan, D. T.; Parkinson, D. Y.; MacDowell, A. A.; Balsara, N. P., Detection of subsurface structures underneath dendrites formed on cycled lithium metal electrodes. *Nat. Mater.* **2014,** *13* (1), 69-73.
19. Monroe, C.; Newman, J., The impact of elastic deformation on deposition kinetics at lithium/polymer interfaces. *J. Electrochem. Soc.* **2005,** *152* (2), A396-A404.
20. Smith, D. M.; Dong, B.; Marron, R. W.; Birnkrant, M. J.; Elabd, Y. A.; Natarajan, L. V.; Tondiglia, V. P.; Bunning, T. J.; Li, C. Y., Tuning Ion Conducting Pathways Using Holographic Polymerization. *Nano Lett.* **2012,** *12* (1), 310-314.
21. Cheng, S.; Li, X.; Zheng, Y.; Smith, D. M.; Li, C. Y., Anisotropic ion transport in 2D polymer single crystal-based solid polymer electrolytes. *Giant* **2020,** *2*, 100021.
22. Cheng, S.; Smith, D. M.; Pan, Q.; Wang, S.; Li, C. Y., Anisotropic ion transport in nanostructured solid polymer electrolytes. *RSC Adv.* **2015,** *5* (60), 48793-48810.
23. Li, X.; Cheng, S.; Zheng, Y.; Li, C. Y., Morphology control in semicrystalline solid polymer electrolytes for lithium batteries. *Mol. Sys. Des. Engin.* **2019,** *4* (4), 793-803.
24. Stone, G.; Mullin, S.; Teran, A.; Hallinan, D.; Minor, A.; Hexemer, A.; Balsara, N., Resolution of the modulus versus adhesion dilemma in solid polymer electrolytes for rechargeable lithium metal batteries. *J. Electrochem. Soc.* **2012,** *159* (3), A222-A227.
25. Khurana, R.; Schaefer, J. L.; Archer, L. A.; Coates, G. W., Suppression of Lithium Dendrite Growth Using Cross-Linked Polyethylene/Poly(ethylene oxide) Electrolytes: A New Approach for Practical Lithium-Metal Polymer Batteries. *J. Am. Chem. Soc.* **2014,** *136* (20), 7395-7402.
26. Pan, Q.; Smith, D. M.; Qi, H.; Wang, S.; Li, C. Y., Hybrid electrolytes with controlled network structures for lithium metal batteries. *Adv. Mater.* **2015,** *27* (39), 5995-6001.
27. Pan, Q.; Barbash, D.; Smith, D. M.; Qi, H.; Gleeson, S. E.; Li, C. Y., Correlating Electrode–Electrolyte Interface and Battery Performance in Hybrid Solid Polymer Electrolyte-Based Lithium Metal Batteries. *Adv. Energy Mater.* **2017,** *7* (22), 1701231.
28. Li, X.; Zheng, Y.; Li, C. Y., Dendrite-free, wide temperature range lithium metal batteries enabled by hybrid network ionic liquids. *Energy Storage Mater.* **2020,** *29*, 273-280.
29. Zheng, Y.; Li, X.; Fullerton, W. R.; Qian, Q.; Shang, M.; Niu, J.; Li, C. Y., Interpenetrating Network-Based Hybrid Solid and Gel Electrolytes for High Voltage Lithium Metal Batteries. *ACS Appl. Energy Mater.* **2021,** *4(6)*, 5639-5648.
30. Zheng, Y.; Li, X.; Li, C. Y., A novel de-coupling solid polymer electrolyte via semi-interpenetrating network for lithium metal battery. *Energy Storage Mater.* **2020,** *29*, 42-51.
31. Li, X.; Zheng, Y.; Duan, Y.; Shang, M.; Niu, J.; Li, C. Y., Designing Comb-Chain Crosslinker-Based Solid Polymer Electrolytes for Additive-Free All-Solid-State Lithium Metal Batteries. *Nano Lett.* **2020,** *20* (9), 6914-6921.
32. Lopez, J.; Sun, Y.; Mackanic, D. G.; Lee, M.; Foudeh, A. M.; Song, M. S.; Cui, Y.; Bao, Z., A Dual-Crosslinking Design for Resilient Lithium-Ion Conductors. *Adv. Mater.* **2018,** *30* (43), 1804142.
33. Li, X.; Zheng, Y.; Pan, Q.; Li, C. Y., Polymerized Ionic Liquid-Containing Interpenetrating Network Solid Polymer Electrolytes for All-Solid-State Lithium Metal Batteries. *ACS Appl. Mater. Inter.* **2019,** *11* (38), 34904-34912.

34. Zheng, Y.; Pan, Q.; Clites, M.; Byles, B. W.; Pomerantseva, E.; Li, C. Y., High-Capacity All-Solid-State Sodium Metal Battery with Hybrid Polymer Electrolytes. *Adv. Energy Mater.* **2018,** *8* (27), 1801885.
35. Rubinstein, M.; Colby, R. H., *Polymer physics*. Oxford university press New York: 2003, 266.
36. Devaux, D.; Bouchet, R.; Glé, D.; Denoyel, R., Mechanism of ion transport in PEO/LiTFSI complexes: Effect of temperature, molecular weight and end groups. *Solid State Ionics* **2012,** *227*, 119-127.
37. Teran, A. A.; Tang, M. H.; Mullin, S. A.; Balsara, N. P., Effect of molecular weight on conductivity of polymer electrolytes. *Solid State Ionics* **2011,** *203* (1), 18-21.
38. Wunderlich, B., *Thermal Analysis of Polymeric Materials*. Springer Berlin Heidelberg: 2005, 783.
39. Mott, P.; Roland, C., Limits to Poisson's ratio in isotropic materials. *Physical review B* **2009,** *80* (13), 132104.
40. Qiu, J.; Liu, X.; Chen, R.; Li, Q.; Wang, Y.; Chen, P.; Gan, L.; Lee, S.-J.; Nordlund, D.; Liu, Y.; Yu, X.; Bai, X.; Li, H.; Chen, L., Enabling Stable Cycling of 4.2 V High-Voltage All-Solid-State Batteries with PEO-Based Solid Electrolyte. *Advanced Functional Materials* **2020,** *30* (22), 1909392.
41. Hallinan, D. T.; Mullin, S. A.; Stone, G. M.; Balsara, N. P., Lithium Metal Stability in Batteries with Block Copolymer Electrolytes. *J. Electrochem. Soc.* **2013,** *160* (3), A464-A470.
42. Liu, K.; Pei, A.; Lee, H. R.; Kong, B.; Liu, N.; Lin, D.; Liu, Y.; Liu, C.; Hsu, P.-c.; Bao, Z., Lithium metal anodes with an adaptive "solid-liquid" interfacial protective layer. *J. Am. Chem. Soc.* **2017,** *139* (13), 4815-4820.
43. Zheng, G.; Wang, C.; Pei, A.; Lopez, J.; Shi, F.; Chen, Z.; Sendek, A. D.; Lee, H.-W.; Lu, Z.; Schneider, H., High-performance lithium metal negative electrode with a soft and flowable polymer coating. *ACS Energy Lett.* **2016,** *1* (6), 1247-1255.
44. Zhu, B.; Jin, Y.; Hu, X.; Zheng, Q.; Zhang, S.; Wang, Q.; Zhu, J., Poly (dimethylsiloxane) Thin Film as a Stable Interfacial Layer for High-Performance Lithium-Metal Battery Anodes. *Adv. Mater.* **2017,** *29* (2), 1603755.
45. Walker, W.; Giordani, V.; Uddin, J.; Bryantsev, V. S.; Chase, G. V.; Addison, D., A Rechargeable Li–O2 Battery Using a Lithium Nitrate/N,N-Dimethylacetamide Electrolyte. *J. Am. Chem. Soc.* **2013,** *135* (6), 2076-2079.
46. Aurbach, D.; Pollak, E.; Elazari, R.; Salitra, G.; Kelley, C. S.; Affinito, J., On the Surface Chemical Aspects of Very High Energy Density, Rechargeable Li–Sulfur Batteries. *J. Electrochem. Soc.* **2009,** *156* (8), A694.
47. Huang, H.; Yin, S.-C.; Nazar, L., Approaching theoretical capacity of LiFePO4 at room temperature at high rates. *Electrochemical Solid-State Letters* **2001,** *4* (10), A170-A172.

TOC: **Decoupling the Modulus and Toughness Effects of Solid Polymer Electrolytes in All Solid-State Lithium Batteries**

*Yongwei Zheng, Xiaowei Li, William R. Fullerton, and Christopher Y. Li**

Department of Materials Science and Engineering, Drexel University, Philadelphia, PA 19104, USA